



# Aeroacoustic analysis of dry ice blasting on divergent nozzle length using CFD to acoustic couple simulation

Mohamad Nur Hidayat Mat<sup>1</sup> · Norzelawati Asmuin<sup>2</sup> · Md Faisal Md Basir<sup>3</sup> · Mashhour A. Alazwari<sup>4</sup> · Mohammad Reza Safaei<sup>4,5</sup>

Received: 10 March 2021 / Accepted: 1 June 2021 / Published online: 27 June 2021  
© Akadémiai Kiadó, Budapest, Hungary 2021

## Abstract

In order to determine the effect of the divergent nozzle length on the single-hose nozzle geometry, the computational couple simulation approach was employed. Furthermore, a model was successfully provided for the two-way exchange of mass, momentum, and energy between two phases. The energy that was exchanged between two involved phases, the solid dry ice particle and a working medium of compressible air-fluid, was also obtained. The model was then coupled with the acoustic programming code solved using the Mump solver. The result revealed that the most extended divergent length showed the highest flow velocity across the nozzle cavity and induced the lowest turbulence flow. Thus, the acoustic sound pressure level was reduced. The shortest divergent nozzle length, equal to 200 mm, produced the highest sound pressure level equal to 85 dBA within the frequency range of 1000 to 1200 Hz. It also produced an average maximum of sound power level, which is 100 dB, across all frequency ranges. Therefore, this study is highly essential since the characteristics of the gas-particle flow within a nozzle cavity provide a deeper understanding of the multiphase flow in turbine and jet engine flow analysis.

**Keywords** Aeroacoustics · CFD · Divergent length · Dry ice blasting · noise · Nozzle geometry

## Introduction

Industrial pollution poses an enormous challenge for plant operators as impurities' existence reduces the device's efficiency, disrupts the involved operation, or even causes certain damages [1]. To combat this problem, a variety of

methods in removing pollutants have been successfully designed and effectively operated [2]. One of these methods is dry ice blasting, wherein a moisture-less condition is required for its operation. The method also substantially produces less waste after cleaning (compared to, for example, sandblasting). Furthermore, its operational parameters can be effortlessly controlled by mass flow and pressure change. On top of that, the dry ice blasting solution is relatively cheap and safe [3]. Nevertheless, this method also has its limitation, which involves its cooling mechanism of the cleaning surface [4].

The dry ice blasting approach is initiated with the air compression and drying stage. Then, the pelleted dry ice (diameter of 3 mm and a length of 5–5 mm) is loaded into a shredder [5]. In cases where smaller dimensions of the pellets are required, they are run through a strainer. A separate system is required to produce the dry ice [6], whether by employing the process as described in [7], or on-site [8], where a pelletizer is utilized to convert the liquid CO<sub>2</sub> into pellets. Once the two-phase dry ice blasting machine is sufficiently loaded with the pellets, the pellets are then blasted to the cleaning surface by the compressed air through a nozzle [9].

✉ Mohammad Reza Safaei  
msafaei@fiu.edu

<sup>1</sup> School of Mechanical Engineering, Faculty of Engineering, Universiti Teknologi Malaysia, 81310 UTM Johor Bahru Johor, Malaysia

<sup>2</sup> Faculty of Mechanical and Manufacturing Engineering, Universiti Tun Hussein Onn, 86400 Parit Raja, Johor, Malaysia

<sup>3</sup> Department of Mathematical Sciences, Faculty of Science, Universiti Teknologi Malaysia, 81310 UTM Johor Bahru Johor, Malaysia

<sup>4</sup> Mechanical Engineering Department, Faculty of Engineering, King Abdulaziz University, Jeddah, Saudi Arabia

<sup>5</sup> Department of Medical Research, China Medical University Hospital, China Medical University, Taichung, Taiwan

The flow parameters are heavily dependent on the air pressure, the mass flow rate of dry ice, as well as the nozzle-surface distance. The system is schematically presented in Fig. 1. Dry ice cleaning is based on three distinct phenomena: abrasion by the flow of kinetic energy, sublimation, and the thermal effect (cooling) [10, 11]. The final force impacting the cleaning surface consists of three different components, namely the force of compressed air, the force of solid CO<sub>2</sub> particles due to their velocity, as well as the sublimation force due to the abrupt changes in the phase as a consequence of the rapid velocity growth [12].

Dry ice blasting is highly beneficial to clean the electrical devices used in aircraft, automobiles, and railway [13]. Even though the method has been previously developed for industrial cleaning purposes, it can also be applied on the surface pretreatment process successfully. For example, it can be used when the aluminum bonding joints [14], or coatings of aluminum oxide [15] or titanium [16], should be improved in terms of adhesive strength. The main component of a dry ice blasting system is the nozzle, and its geometry substantially influences the two-phase flow outlet parameters and the cleaning speed, consequently [17]. More specifically, a supersonic two-phase flow is a phenomenon modeled in this study. Previous studies have reported a two-phase flow while passing through a convergent-divergent nozzle. Using the Laval nozzle, one of these studies has proposed a model for the mixture of air and water [18, 19]. A simulation of high-speed fluid mix with a particle is very challenging, especially in large density gradients, and requires a proper computational model. A study done by Bonelli et al. [20] has shown a method to minimize the computational load by using the localized artificial diffusivity (LAD) model. The model is used to suppress the unresolved high-frequency modes of the flow field and accounts for the effects of the subgrid scale on the resolved variables by adding artificial fluid transport coefficients to the physical ones. The theory was then developed and extended by Kawai, Lele [21]. Apart from that, some studies have examined the nozzles explicitly designed for dry ice blasting purposes, where the nozzle shapes were analyzed to determine the generated operational noise due to the nozzle geometry [19].

Nonetheless, to the best of the authors' knowledge, there is little or no study was investigating the substantial effect of nozzle geometry on the dry ice blasting process's performance characteristic in terms of divergent length [22, 23]. In a previous study, the convergent peripheral section's effect was not considered in analyzing the two-dimensional model of a nozzle geometry [19]. This is essential since the reference nozzle was a dual-hose nozzle geometry with an asymmetrical shape [24].

As an attempt to fill this knowledge gap, a three-dimensional single-hose nozzle geometry has been investigated. This was done to examine the relationship between different divergent nozzle lengths, 50 mm increment in a range of 200 to 400 mm, and the flow characteristic. Therefore, a novelty approach was employed in this research to investigate the flow characteristic inside the nozzle geometry of dry ice blasting with dual hoses by utilizing a three-dimensional model and coupling it with an acoustic study in which an aeroacoustic analysis on the sound generation over different divergent nozzle lengths. Upon finding the characteristics of divergent nozzle length concerning acoustic sound power level generation, this application can be applied to dry ice blasting fabricator to create a nozzle geometry with a specific dimension to minimize sound pressure level when dealing with the cleaning of office flow where the requirement of low-level noise is compulsory.

## Model implementation

### Mathematical model

General Equations.

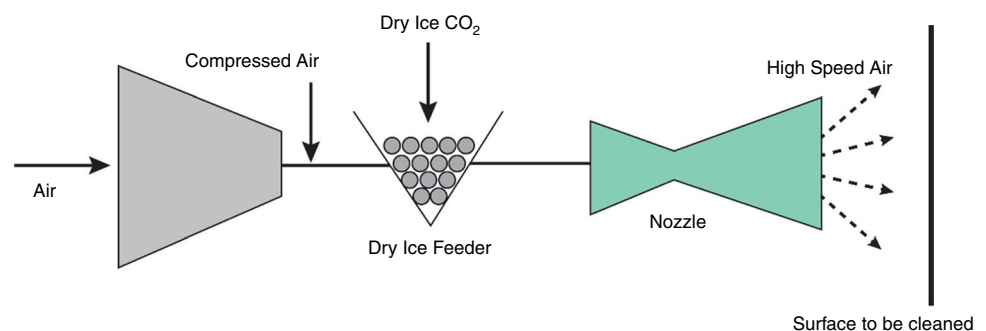
The numerical model developed for the continuous phase was based on the following equations:

Energy [25, 26]:

$$\frac{\partial}{\partial t}(\rho H) + \frac{\partial}{\partial x_j} \left( \rho u_j H + u_j p - k \frac{\partial T}{\partial x_j} - u_j \sigma_{ij} \right) = 0 \quad (1)$$

Momentum [26, 27]:

**Fig. 1** Process flow of dry ice cleaning system



$$\frac{\partial}{\partial t}(\rho u_j) + \frac{\partial}{\partial x_j}(\rho u_i u_j + p \delta_{ij} - \sigma_{ij}) = 0 \tag{2}$$

where we can write the viscous stress tensor as [26, 28]:

$$\sigma_{ij} = \mu \left( \frac{\partial u_i}{\partial x_j} + \frac{\partial u_j}{\partial x_i} \right) - \frac{2}{3} \mu \frac{\partial u_k}{\partial x_k} \delta_{ij} \tag{3}$$

Continuity [26, 29]:

$$\frac{\partial \rho}{\partial t} + \frac{\partial}{\partial x_j}(\rho u_j) = 0 \tag{4}$$

Ideal gas law:

$$p = \rho RT \tag{5}$$

where we can write the total molecular viscosity as:

$$\mu = \mu_0 + \mu_t \tag{6}$$

Then, the molecular viscosity was summed up with the turbulent eddy viscosity to express the effective fluid viscosity [26, 30]:

$$\frac{\partial k}{\partial t} + U_j \frac{\partial k}{\partial x_j} = P_k - \beta^* k \omega + \frac{\partial}{\partial x_j} \left[ (v + \sigma_k \nu_T) \frac{\partial k}{\partial x_j} \right] \tag{7}$$

On the other hand, the dry ice particles consider a discrete particle that requires a discontinuous equation. The particles are assumed to be spherical for simplicity. One-way coupling is assumed between the particle and airflow fields, and the interaction between particles is neglected because the particle flow is dilute. The general form of the trajectory equation for a single particle with constant mass is given as [26]:

$$\frac{dU_p}{dt} = \frac{1}{\tau_p} v_{rel} n_{rel} \tag{8}$$

$$\frac{dX_p}{dt} = U_p \tag{9}$$

The development of the total energy heat transfer model was accomplished by determining the high-speed flow value (Mach number > 0.3) along with the compressibility effects of the system.

### Large Eddy simulation

Large Eddy simulation (LES) was utilized in this study to accurately model the turbulence flow after mapping results from the RANS analysis [31]. The LES technique for simulating turbulent flow used grid mesh as the filter. Filtering is the convolution of a function with a filtering kernel G presented as [32]:

$$\bar{u}_i(\bar{x}) = \int G(\bar{x} - \bar{\xi}) u(\bar{\xi}) d\bar{\xi} \tag{10}$$

$$u_i = \bar{u}_i + u'_i \tag{11}$$

Which results in a total velocity of  $u_i$ , while the term  $\bar{u}_i$  represents the resolvable scale part, and  $u'_i$  describes the subgrid-scale part. Based on this equation, the new value of  $u_i$  can be substituted for all governing equations as presented above.

### Geometrical modeling

Dry ice nozzle geometry is designed using scFLOW pre-processor, a cradle product, as shown in Fig. 2. The notation dimension of a dry ice blasting nozzle is illustrated in the figure. Nozzle parameters consist of the length and diameter of the convergent nozzle ( $l_{co}$  and  $d_{co}$ ), the diameter of the gas inlet ( $d_{ig}$ ), as well as its insertion length in the convergent section ( $l_{ig}$ ). Other parameters can be listed as the diameters of dry ice inlet ( $d_{ip}$ ) and throat ( $d_{th}$ ), the divergent length ( $l_{di}$ ), and the exit width and height ( $w_{ex}$  and  $h_{ex}$ ). The area ratio of the nozzle exit to the throat is defined as the expansion ratio. Table 1 presents the properties corresponding to the dry ice solid particle.

Fig. 2 Schematic diagram of dry ice blasting nozzle geometry

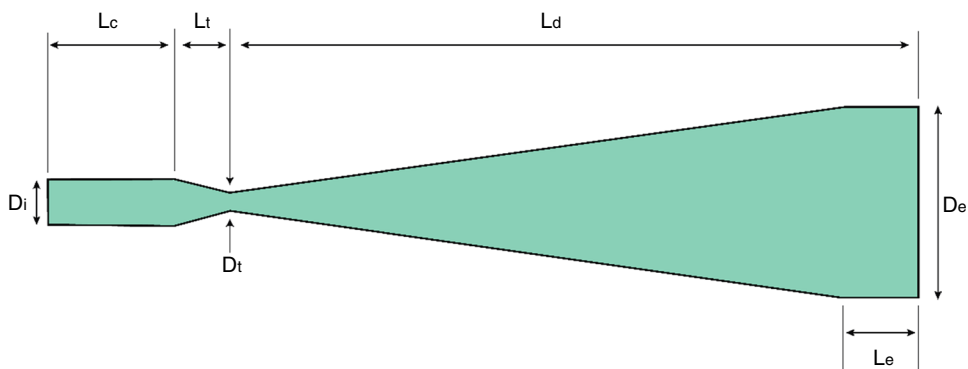


**Table 1** The properties of dry ice pellets [11]

Parameters	Values
Temperature/ $^{\circ}\text{C}$	78.50
Density / $\text{Kg m}^{-3}$	1560
Heat capacity / $\text{Jkg}^{-1} \text{K}^{-1}$	519.16
Shape factor	0.76

### Mesh for DIB nozzle geometry

In this process, the finite volume method was employed in CFD simulation code [33, 34]. Thus, the computational domain was required to be meshed to solve the governing equation for every cell [35–37]. The mesh model is presented in Fig. 3. Poly-mesh is used by the programming code in scFLOW [27]. This mesh type significantly benefits the model, as every cell has many neighboring regions [38–40]. Hence, the gradients can be approximated successfully. Apart from that, since the polyhedrons are less sensitive to stretching than the tetrahedrons, a better mesh quality is produced [41, 42].

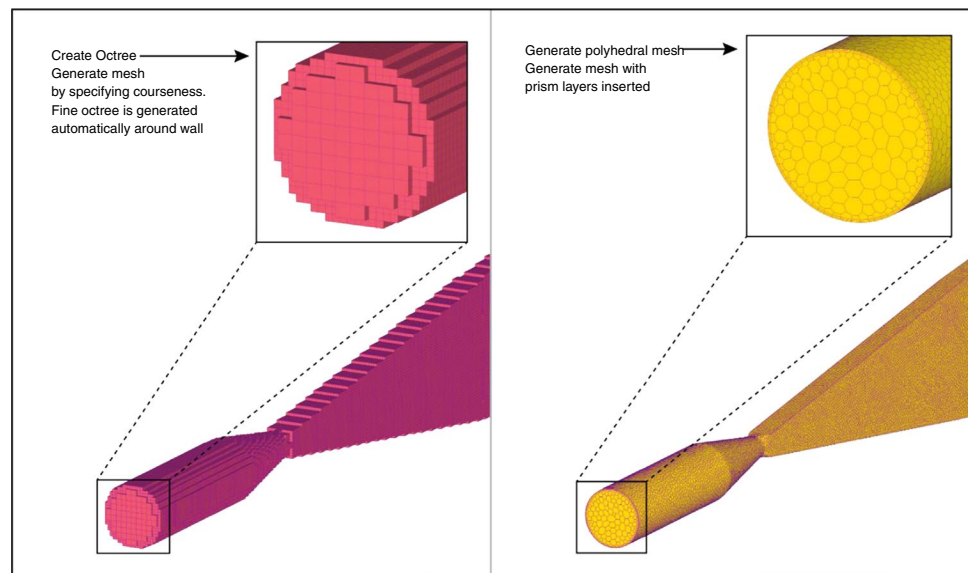
Consequently, this causes the numerical stability of the model to be improved [43–45]. Furthermore, the small mesh is used for significant gradient changes, while for other purposes, the coarse mesh is utilized instead [46–48]. It is essential to maintain an optimum mesh quality for accuracy and stability [49–52]. However, the computational load must not be increased too much. Besides, the process of generat-

control command by the octree parameter. Two-wall prism layers are also set to the nozzle surface with a thickness coefficient of 0.2. Thus, a 2.4 mm wall thickness is set around the wall layer to capture the boundary viscous sublayer. The RANS method is initiated at the first simulation to determine the suitable element size. The first grid point from the wall is within the viscous sublayer (e.g.,  $y^+ < 5$ ). As a clarification, the poly-mesh is applied to adapt the unstructured mesh property on the nozzle surface [53, 54].

### Mesh sensitivity study

The numerical accuracy of CFD modeling directly relates to mesh property. The present approach employs the finite volume method in which the model needs to be discretized into mesh elements with different mesh sizes to adapt to different shapes and geometry [55, 56]. However, different mesh sizes in the model give different results due to different accuracy. Thus, mesh sensitivity is crucial to be determined at an early stage before being further analyzed. The mesh sensitivity of the present study is shown in Table 2. The table consists of 3 different categories of mesh, which are coarse, medium, and fine. Fine mesh represents smaller-sized mesh in the model, and it turns out to have the biggest number of mesh. The fixed measurement result is taken from the nozzle outlet velocity. The 3 mesh categories are presented along with extrapolated error and extrapolated velocity as a reference and ideal mesh size. Extrapolated velocity is the

**Fig. 3** Polyhedral mesh generated by defining the octree parameter



ing mesh is controlled by the octree parameter. The restricted minimum and maximum octant sizes are set to be 12 mm. The surface mesh around the nozzle geometry is set to be 1 mm. The poly-mesh is then generated by following the

outlet velocity when the mesh size is infinitely very small, which is the mesh size approaching zero. Therefore, this study utilizes fine mesh that provides less than 5% errors compared to extrapolated velocity.

**Table 2** Mesh sensitivity study of nozzle geometry

Mesh type	Representative cell length/mm	Number of mesh	Outlet velocity	Extrapolated outlet velocity (h=0)	Extrapolated error/%
Fine	6.30	136,320	78.64		4.41
Medium	12.29	58,536	84.32	75.32	11.95
Course	19.53	4310	104.51		38.75

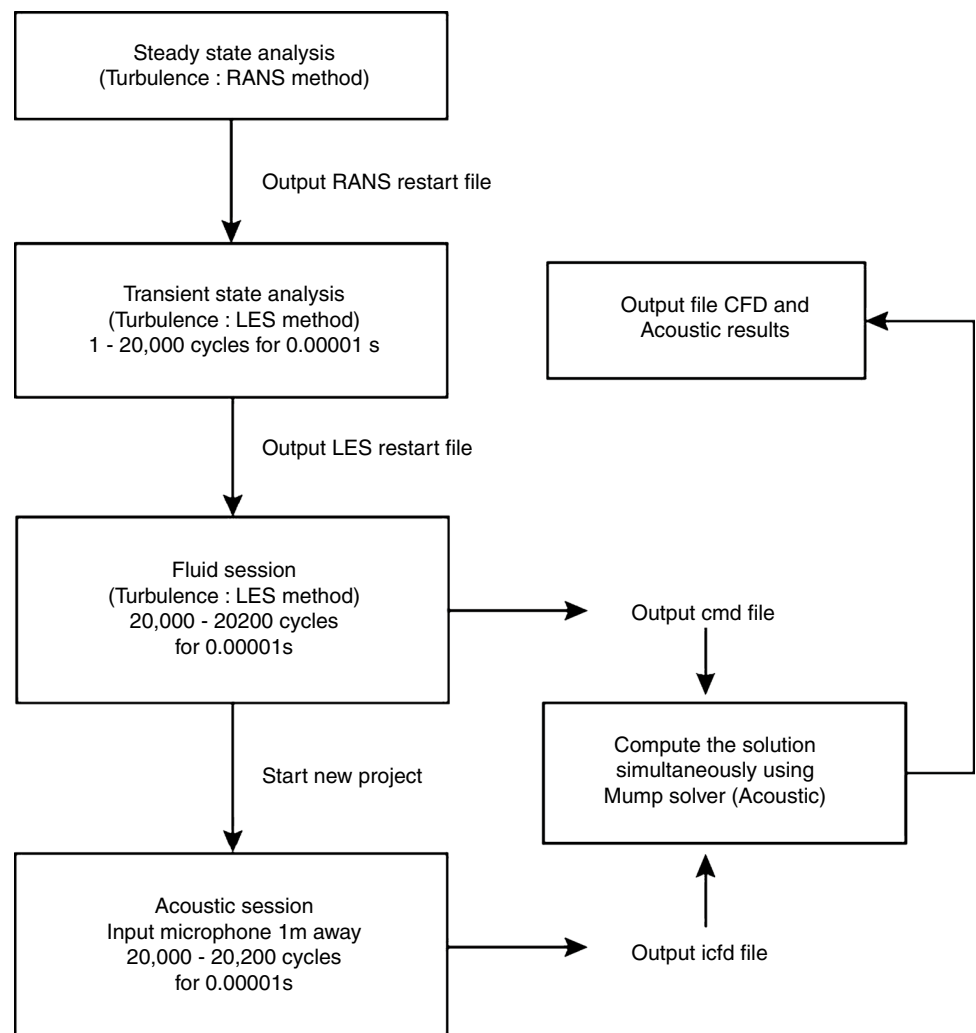
### CFD—acoustic couple simulation method

In this method, an investigation on the acoustic property of DIB nozzle was conducted using an aeroacoustic simulation approach. The first step in performing the couple simulation was by conducting the steady-state analysis using the Reynolds Average Navier Stokes (RANS) method to represent the turbulent model [57, 58] as shown in Fig. 4. The RANS method is a time-averaged equation of motion for fluid flow. The idea behind using this scheme first in this couple simulation is because of the mapping function. The mapping function

requires finding the suitable courant number associated with nozzle geometry. Thus, a better time step can be predicted for high accuracy in LES scheme. The solution was computed over 200 cycles and converged at 120 cycles. The setup criteria for the relative errors of those governing equations were less than  $1 \times 10^{-4}$ . During the steady-state analysis, particle tracking was not activated to let the flow reach the steady state before the particle (dry ice pallet) was introduced.

Once the steady-state solution had converged, the RANS method was then replaced by the large Eddy simulation (LES) method [59] by selecting a transient analysis over 20,000

**Fig. 4** The flowchart of coupling CFD to acoustic simulation process



cycles. LES scheme is a mathematical model for turbulence analysis. LES requires a high computational load but has a better sense of mathematical accuracy to capture eddy's turbulence flow which is bigger than the meshing element. During the LES method, a fluid session was activated in scFLOW-pre to couple the CFD to the acoustic file configuration. The acoustic session was then activated when the output CMB file from the fluid session was generated. In the acoustic session, the acoustic boundary condition was required to be set up by providing the property of an infinite element, acoustic source, and frequency of measurement. Finally, the program would generate an acoustic file to perform the linked simulation between CFD and acoustic simultaneously.

### The validation of the model

The numerical value of output velocity from a nozzle geometry carried out by Dzido et al. [11] was used in the present model validation study as shown in Table 3. In this process, the cleaning time was vitally influenced by the outlet flow velocity. For the experimental setup, cleaning the given surface was carried out from two distinct distances of 15 and 30 cm. Apart from that, the cleaning time was also measured and recorded. The first test included a sheet made out of steel covered with synthetic paint, an inlet pressure, and a dry ice mass flow rate equal to 5 bar and  $48 \text{ kg h}^{-1}$ , respectively.

Meanwhile, a surface made from ceramic covered with flour containing wallpaper glue, along with an inlet pressure and a dry ice mass flow rate equal to 3 bar and  $40 \text{ kg h}^{-1}$ , respectively, is utilized in the second test. Table 3 presents the validation results generated. It can be seen that the maximum relative error is 0.34%, and the minimum error is 0.15%.

## Results and discussions

### Gas—particle flow characteristic along the nozzle centerline

The flow properties of the gas-particle mixture passing through a nozzle cavity were measured from a nozzle inlet up to the outlet. The result can be seen in Fig. 5. The simulation was carried out for five divergent nozzle lengths, with 50 mm increment in a 200–400 mm range. Figure 5a presents the pressure distribution of the gas particle on the centerline. It can be witnessed that there is a decrease in the trend of the graph as the distance from the inlet increases until it reaches 75 mm. This location is known to be the throat section. After reaching the throat section, the trend increases slightly. The drop of pressure then occurs in the throat section due to the gradual changes in geometry size. Thus, this increases the friction of the fluid flow. It is also found that the divergent length of 200 mm produces the

lowest pressure distribution compared to other divergent nozzle lengths.

Besides, the eddy viscosity coefficient is an essential parameter in designing an optimum nozzle geometry. Eddy viscosity is shear stress within a turbulent flow of compressed air to the vertical gradient velocity. Figure 5b shows the result of the eddy viscosity coefficient against the distance from the nozzle inlet. The pattern of the graph is sideways until it reaches the nozzle outlet at 200 mm. It can also be seen that there is a sudden increase in the value at 200 mm of divergent length. This occurs because the nozzle outlet is very close to the atmosphere. Thus, this causes a disturbance near the outlet of the nozzle. Apart from that, the dry ice blasting media operate at the lowest temperature, which is below  $-78.5 \text{ }^\circ\text{C}$ . This is important to ensure that the process can sustain and hold the particle's lowest temperature until it reaches the cleaning surface. Figure 5c presents the result of the temperature of airflow along the nozzle cavity. It is found that the trend of the graph increases as it reaches the throat section and decreases afterward. The higher temperature at the throat section is due to the friction of air and particles colliding at the wall. This friction causes the heat energy to be released near the throat section, as indicated at the distance of 75 mm from the nozzle inlet.

On the other hand, the turbulence dissipation rate is positively related to the heat distribution along with the nozzle, which affects the temperature inside the nozzle. The turbulence dissipation rate is observed when the turbulence energy is absorbed by breaking down the eddies into smaller eddies until it is ultimately converted into heat by viscous forces. The result of the turbulence dissipation rate is presented in Fig. 5d. It is found that the pattern of the graph is sideways, except for the divergent length of 200 mm. This nozzle gives the highest value of turbulence dissipation rate at a distance of 150 mm from the inlet. The conversion rate near the outlet is much faster due to the temperature at the outlet. Since the endpoint of the divergent length of 200 mm is very close to the atmosphere, the heat being absorbed is faster than other divergent nozzle lengths. Next, Fig. 5e presents the result of turbulence energy versus the distance from the nozzle inlet. It is found that the trend is increasing slightly. However, the nozzle with a divergent length of 200 mm shows a tremendous increase in its value at 150 mm nozzle location from the inlet. This is due to the disturbance taking place near the nozzle outlet.

Consequently, this increases the turbulence energy at the outlet section. Figure 5f shows the result of vorticity against the distance from the nozzle inlet. It is found that the pattern for all the divergent nozzle lengths is sideways except for 200 mm. It also causes a spike in the value of vorticity at a distance of 150 mm from the nozzle inlet. Vorticity is a vector field that provides a local measure of a fluid parcel's instantaneous rotation across the fluid continuum. The



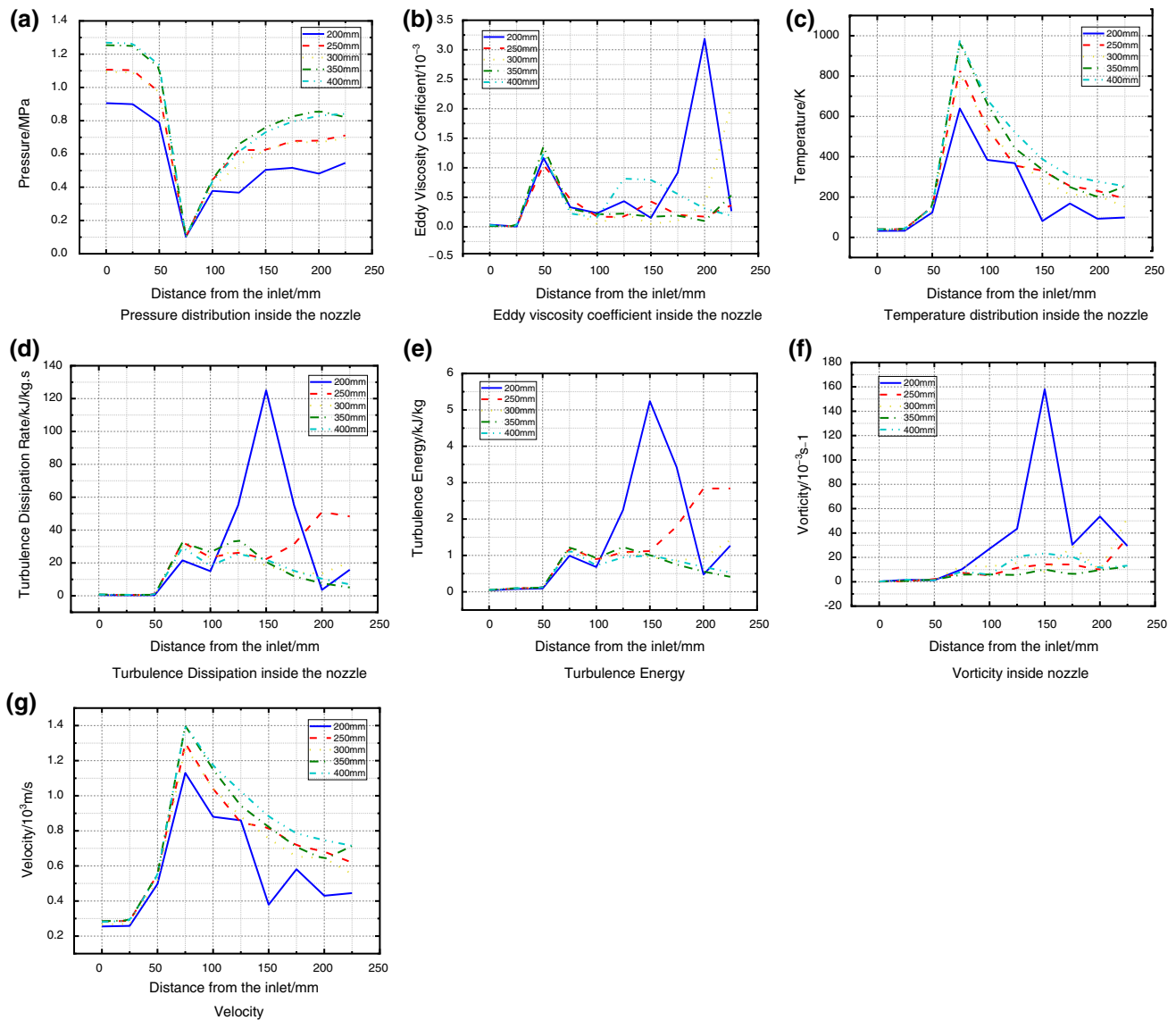


Fig. 5 The development of gas-particle flow along the centerline axis

Table 3 Validation data, compared with Dzido et al. [11] results

Distance from nozzle outlet	Flow rate/kg h <sup>-1</sup>	Pressure/bar	Experimental velocity/m s <sup>-1</sup>	Simulation velocity/m s <sup>-1</sup>	Relative errors/%
15 cm	48	5	75.77	75.65	0.15
30 cm	48	5	58.94	59.06	0.20
15 cm	40	3	115.48	115.87	0.34
30 cm	40	3	85.8	85.95	0.17

increase in vorticity for all nozzle outlets is due to the incoming air's disturbance to the nozzle outlet. Thus, this contributes to the air vorticity near the nozzle outlet region. Apart from the vorticity, the velocity increase also contributes to flow disturbance near the outlet region. Figure 5g shows the result of the velocity across the nozzle centerline. It is

found that the trend of the graph is inversely proportional to the pressure distribution, as shown in Fig. 5a. The maximum velocity seems to occur at the throat section, located at 75 mm from the inlet. The airflow reaching the throat is gradually decreasing in the cross-sectional area. Thus, the flow is choked, and its speed at the throat section eventually

reaches the speed of sound, which is equivalent to the Mach number of one. This speed is considered a sonic speed.

### Real-time velocity of an airflow across the nozzle cavity

The stability of DIB operation is crucial as the dry ice cleaning process is performed. Having a constant particle flow to the cleaning surface affects the cleaning efficiency of the system. Thus, Fig. 6 presents the real-time velocity value at the throat and outlet nozzle regions. Figure 6a shows the investigation result of the throat section's velocity for all divergent nozzle lengths. It is found that the trend of the velocity decreases drastically before reaching 100 cycles. The simulation is conducted at 400 cycles, and each cycle has a time step of 0.00001 s. Therefore, in this case, the value of the velocity across all divergent nozzle lengths drops at the time of 0.001 s. After the completion of this cycle, the value of the velocity trend becomes sideways. This shows that the stability of operation starts to happen at 100 cycles. This is because particle velocity flow becomes constant as the time is taken or the number of cycles increases.

On the other hand, the velocity is recorded at the nozzle outlet for all nozzle divergent lengths, as shown in Fig. 6b. The trend of the outlet velocity is  $x$  due to the turbulence factors. Since the nozzle flow outlet is the nearest to the atmosphere, this affects the flow velocity as well. Having smooth and concentrated velocity at the outlet is paramount in DIB operation to sustain the highest cleaning efficiency. After 100 cycles, the outlet velocity reaches a stable value and becomes more stable since then. Thus, it can be concluded that the stable operation to perform DIB cleaning process takes 100 cycles or 0.001 s.

### Acoustic characteristic

The acoustic pattern inside the nozzle geometry was investigated through a simulation method using acoustic software known as Actran. The results of the acoustic characteristics are presented qualitatively and quantitatively. The qualitative method shows the sound pressure level (SPL) contour plot development inside the nozzle cavity, as in Fig. 7. The SPL measurement is taken under 14,000 Hz of the frequency range, and the unit used is dBA, which stands for decibel A-weighting. SPL's contour plot development is taken in the middle of the nozzle by having a cut-half plane section view. It is found that the maximum SPL development occurs at 100 dBA at the tip of the nozzle outlet, as presented in the red contour region. Other than that, the shortest divergent length of 200 mm develops the highest SPL intensity compared to other divergent lengths in which the red color contour intensity occurs from the nozzle outlet to the nozzle throat section. The highest intensity development that

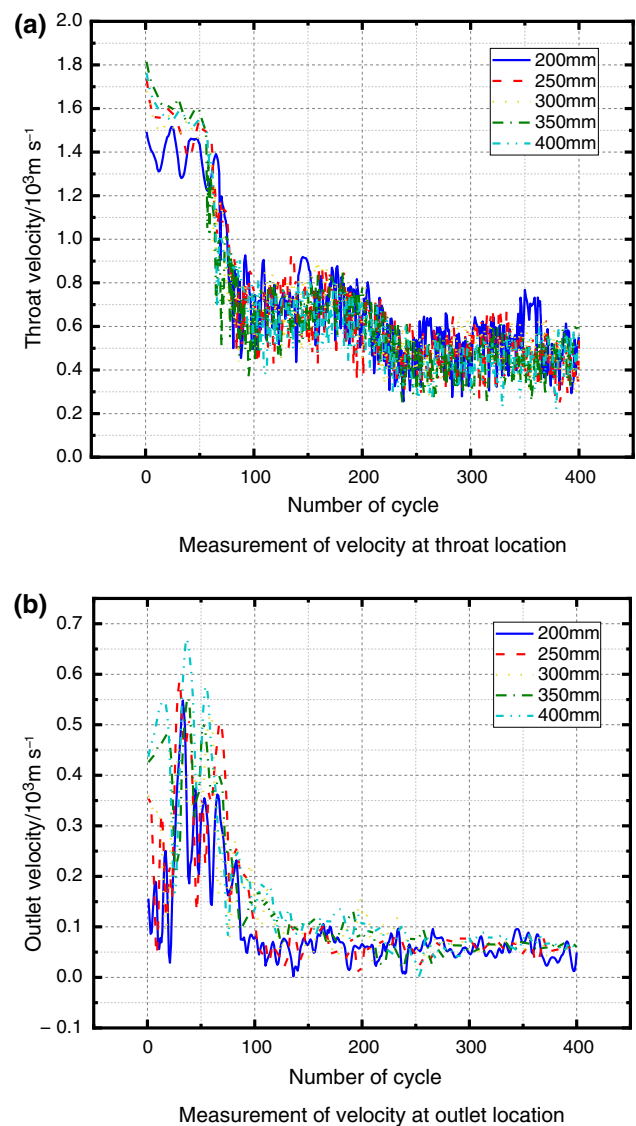


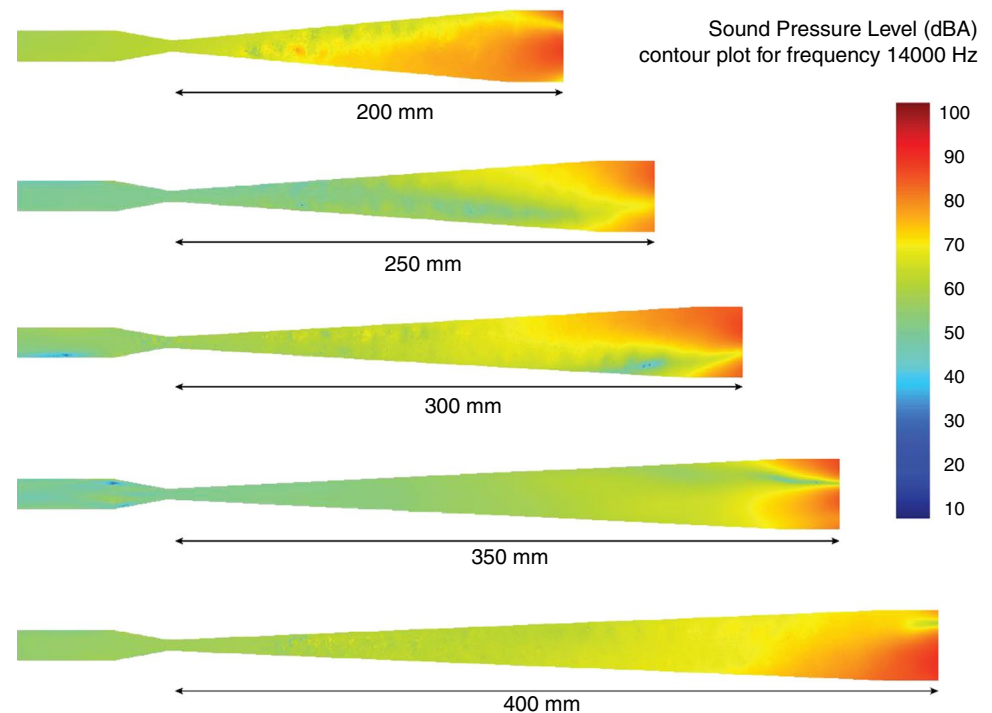
Fig. 6 Real-time velocity development along the nozzle cavity

mainly occurs for all divergent nozzle lengths is due to the nozzle outlet's turbulence development. Since the outlet nozzle is exposed to the atmosphere region, disturbance happens, which then induces acoustic noise near the region. To support this claim, Fig. 5e shows the turbulence energy development in the nozzle centerline. Apart from the highest SPL value, the blue contour plot representing the lowest SPL emission ranging from 10 to 40 dBA presented at divergent nozzle lengths of 300 and 350 mm. The location of occurring lowest SPL value is at the convergent and divergent section. On average, the SPL ranging from 50 to 60 dBA is the most common sound occurring for all divergent nozzle sections, especially at the throat section.

The value of its turbulence boosts as the nozzle inlet increases. Besides, the results of the quantitative method are



**Fig. 7** The contour plot of sound pressure level



also presented in Fig. 8. The results of the acoustic intensity, which are the sound pressure level (dBA), sound power level (dB), flow pressure (Pa), and directivity, are plotted against different frequency ranges in the log scale. The sound measurement is done by introducing one microphone at one meter away from the nozzle that acts as the noise source. This method of measurement refers to ISO 3746 under the survey-grade method. Under this standard, the noise is placed under a free field condition. Thus, Actran has the capability to define those regions as an infinite element. This infinite element is represented as a non-reflecting boundary condition. Figure 8a shows the sound pressure level (dBA) against the frequency range in the log scale. It is found that the maximum value of SPL for all divergent nozzle lengths occurs between 1000 and 1200 Hz of the frequency range. Also, the divergent nozzle length gives SPL the highest value over the frequency range compared to others.

In contrast, the divergent nozzle length of 400 mm provides the lowest value of SPL as it is operated near 10,000 Hz of frequency range. It is also important to note that the sound power level is crucial in defining the noise source. Sound power level is a measure of the acoustic energy emitted from a noise source, expressed in decibels. Figure 8b demonstrates the sound power level (dB) against the frequency range in the log scale. The result shows that the average maximum value of the sound power level is

110 dB across all frequency ranges. The pattern of sound power level produced for all divergent lengths is sideways and zigzag in nature with increasing value of frequency range.

Furthermore, the flow pressure of all divergent nozzle lengths is presented in Fig. 8c. It is found that below 10,000 Hz, the flow pressure has negative and positive values. The negative value of the flow pressure indicates that the pressure is below the human hearing mechanism. Thus, humans are unable to hear the sound pressure. Another important finding shows that, within the frequency range of 1000–10,000 Hz, the value of flow pressure is higher, especially for divergent nozzle length of 250 mm. Apart from that, the directivity plot is presented in Fig. 8d. The directivity plot is an essential source in finding the direction of the noise generated over 360 degrees. Figure 8d shows the result of the directivity plot against different angles up to 360 degrees. It is found that the maximum sound pressure level develops within the angle of 90°, 270°, 135°, and 315°. The highest acoustic sound pressure level occurs at the nozzle with a divergent length of 250 mm. In summary, the shortest divergent emits the highest acoustic noise source across all frequency ranges.

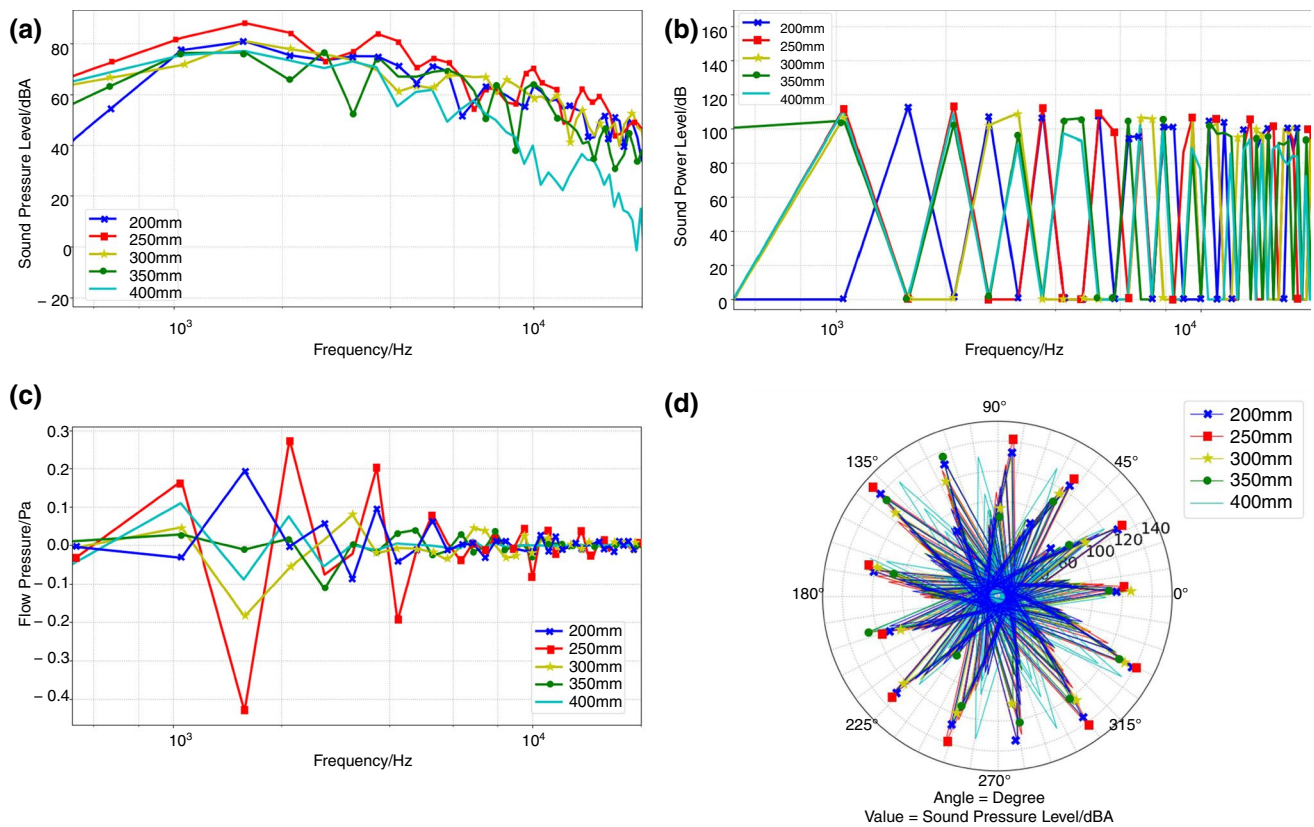


**Fig. 8** Acoustic sound characteristic of divergent length

## Conclusions

In this study, the gas particles flowing along the nozzle centerline were simulated and analyzed. This was done with a steady flow, focusing on the nozzle geometry of a 3D dry ice blasting with dual hoses. Apart from that, a 3D simulation was carried out for six different divergent nozzle lengths. In conclusion, it was found from the simulation results that:

- The development of the pressure along the nozzle centerline was minimum at the location of the nozzle throat.
- Eddy viscosity, turbulence dissipation rate, vorticity, and turbulence energy have the highest development at the nozzle outlet's end due to the nearest air atmosphere's disturbance.
- The highest temperature development occurred in the throat section due to the gradual decrease in the cross-sectional area's sizing that induced friction.
- The highest velocity occurred at the nozzle throat since the cross-sectional area was at its minimum, where the gas velocity locally became sonic.
- The stability of DIB operation occurred after 0.001 s since the velocity became stable and constant.

- The sound pressure level mainly occurred at the tip of the nozzle outlet for all divergent nozzle lengths, as presented in the result of the sound pressure level contour plot.
- The maximum sound pressure level measured at the microphone 1 m away was 85 dBA for the shortest nozzle divergent length of 200 mm, while the minimum sound pressure level occurred for nozzle divergent length of 400 mm after 1400 Hz of frequency.
- The average maximum sound power level for all nozzle divergent lengths was 110 dB across all frequency ranges.

Hence, these results conclude that gas-particles' characteristics inside the nozzle cavity are indeed impacted by changing the nozzle divergent length in a single nozzle geometry.

**Acknowledgements** This project was supported by the Ministry of Higher Education Malaysia for supporting this research under Fundamental Research Grant Scheme Vot No. FRGS/1/2018/TK10/UTHM/02/15 and the authors would like to express gratitude to MSC Software Corporation for allowing the authors to use their commercial CFD and Acoustic software, which are scFLOW and Actran, to perform the aeroacoustics analysis.

**Author contributions** MNHM, NA, and MFMB were involved in conceptualization, data curation, investigation, methodology, formal analysis, validation, and software; MAA and MRS helped in project administration, funding acquisition, writing—review and editing, and supervision. All authors have read and agreed to the published version of the manuscript.

## Declarations

**Conflict of interest** The authors declare no conflicts of interest.

## References

- Wang N, Choi Y. Challenges for sustainable water use in the urban industry of Korea based on the global non-radial directional distance function model. *Sustainability*. 2019;11(14):3895.
- Katheresan V, Kansedo J, Lau SY. Efficiency of various recent wastewater dye removal methods: a review. *J Environ Chem Eng*. 2018;6(4):4676–97.
- Zhou W, Liu M, Liu S, Peng M, Yu J, Zhou C. On the mechanism of insulator cleaning using dry ice. *IEEE Trans Dielectr Electr Insul*. 2012;19(5):1715–22.
- Sherman R, Grob J, Whitlock W. Dry surface cleaning using CO<sub>2</sub> snow. *J Vacuum Sci Technol B: Microelectron Nanom Struct Process, Measure, Phenomena*. 1991;9(4):1970–7.
- Máša V, Kuba P. Efficient use of compressed air for dry ice blasting. *J Clean Prod*. 2016;111:76–84.
- Górecki J, Malujda I, Wilczyński D, editors. The influence of geometrical parameters of the forming channel on the boundary value of the axial force in the agglomeration process of dry ice. *MATEC Web of Conferences*; 2019: EDP Sciences. 254:05001, <https://doi.org/10.1051/mateconf/201925405001>
- Zhang X-R, Yamaguchi H. An experimental study on heat transfer of CO<sub>2</sub> solid–gas two phase flow with dry ice sublimation. *Int J Therm Sci*. 2011;50(11):2228–34.
- Liu Y-H, Maruyama H, Matsusaka S. Effect of particle impact on surface cleaning using dry ice jet. *Aerosol Sci Technol*. 2011;45(12):1519–27.
- Liu Y-H, Hiram D, Matsusaka S. Particle removal process during application of impinging dry ice jet. *Powder Technol*. 2012;217:607–13.
- Uhlmann E, Spur G, Elbing F, editors. Development of flexible automatic disassembly processes and cleaning technologies for the recycling of consumer goods. *Proceedings of the 2001 IEEE International Symposium on Assembly and Task Planning (ISATP2001)*. Assembly and Disassembly in the Twenty-first Century. (Cat. No. 01TH8560); 2001: IEEE. pp. 442–446, <https://doi.org/10.1109/ISATP.2001.929074>.
- Dzido A, Krawczyk P, Kurkus-Gruszecka M. Numerical analysis of dry ice blasting convergent-divergent supersonic nozzle. *Energies*. 2019;12(24):4787.
- Spur G, Uhlmann E, Elbing F. Dry-ice blasting for cleaning: process, optimization and application. *Wear*. 1999;233:402–11.
- Máša V, Kuba P, Petrilák D, Lokaj J. Decrease in consumption of compressed air in dry ice blasting machine. *Chem Eng*. 2014;39:805–10.
- Elbing F, Anagreh N, Dorn L, Uhlmann E. Dry ice blasting as pretreatment of aluminum surfaces to improve the adhesive strength of aluminum bonding joints. *Int J Adhes Adhes*. 2003;23(1):69–79.
- Dong S, Song B, Hansz B, Liao H, Coddet C. Study on the mechanism of adhesion improvement using dry-ice blasting for plasma-sprayed Al<sub>2</sub>O<sub>3</sub> coatings. *J Therm Spray Technol*. 2013;22(2–3):213–20.
- Dong S, Liao H. Substrate pre-treatment by dry-ice blasting and cold spraying of titanium. *Surf Eng*. 2018;34(3):173–80.
- Mat MNH, Asmuin NZ, Basir MFM, Goodarzi M, Hasan NH. Effect of impact force for dual-hose dry blasting nozzle geometry for various pressure and distance: an experimental work. *Eur Phys J Plus*. 2020;135(2):260.
- Mat MNH, Asmuin NZ, Basir MFM, Safaei MR, Kasihmuddin MSM, Khairuddin TKA, et al. Optimizing nozzle convergent angle using central composite design on the particle velocity and acoustic power level for single hose dry ice blasting nozzle. *J Therm Anal Calorim*. 2020. <https://doi.org/10.1007/s10973-020-10083-5>.
- Mat MNH, Asmuin NZ, Hasan NH, Zakaria H, Rahman M, Khairulfaad R, et al. Optimizing dry ice blasting nozzle divergent length using CFD for noise reduction. *CFD Lett*. 2019;11:18–26.
- Bonelli F, Viggiano A, Magi V. How does a high density ratio affect the near-and intermediate-field of high-Re hydrogen jets? *Int J Hydrogen Energy*. 2016;41(33):15007–25.
- Kawai S, Lele SK. Localized artificial diffusivity scheme for discontinuity capturing on curvilinear meshes. *J Comput Phys*. 2008;227(22):9498–526.
- Raef T, Elzahaby A, Khalil M, editors. Enhancement of propulsion performance through jet noise reduction technologies: a review. *Proceedings of the 16th Int. AMME Conference*; 2014.
- Alam M, Setoguchi T, Matsuo S, Kim H. Nozzle geometry variations on the discharge coefficient. *Propuls Power Res*. 2016;5(1):22–33.
- Mat MNH, Asmuin N. Optimizing nozzle geometry of dry ice blasting using CFD for the reduction of noise emission. *Int J Integr Eng*. 2018. <https://doi.org/10.30880/ijie.2018.10.05.019>
- Dadsetani R, Salimpour MR, Tavakoli MR, Goodarzi M, Bandarra Filho EP. Thermal and mechanical design of reverting microchannels for cooling disk-shaped electronic parts using constructal theory. *Int J Numer Methods Heat Fluid Flow*. 2019;30:245–65.
- Anderson JD. Governing equations of fluid dynamics. *Comput Fluid Dyn*. 1992. [https://doi.org/10.1007/978-3-662-11350-9\\_2](https://doi.org/10.1007/978-3-662-11350-9_2).
- Ettaleb A, Abbassi MA, Farhat H, Guedri K, Omri A, Borjini MN, et al. Radiation heat transfer in a complex geometry containing anisotropically-scattering mie particles. *Energies*. 2019;12(20):3986.
- Rozati, S.A., Montazerifar, F., Ali Akbari, O., Hoseinzadeh, S., Nikkhal, V., Marzban, A., Abdolvand, H. and Goodarzi, M. Natural convection heat transfer of water/Ag nanofluid inside an elliptical enclosure with different attack angles. *Math. Methods Appl. Sci*. 2020. 1–18. <https://doi.org/10.1002/mma.7036>
- Dadsetani R, Sheikhzadeh GA, Safaei MR, Leon AS, Goodarzi M. Cooling enhancement and stress reduction optimization of disk-shaped electronic components using nanofluids. *Symmetry*. 2020;12(6):931.
- Abdulrazzaq T, Togun H, Goodarzi M, Kazi S, Ariffin M, Adam N, et al. Turbulent heat transfer and nanofluid flow in an annular cylinder with sudden reduction. *J Therm Anal Calorim*. 2020;141:1–13.
- Zahabi H, Torabi M, Alamatian E, Bahiraei M, Goodarzi M. Effects of geometry and hydraulic characteristics of shallow reservoirs on sediment entrapment. *Water*. 2018;10(12):1725.
- Garnier E, Adams N, Sagaut P. *Les governing equations large eddy simulation for compressible flows*. New York: Springer; 2009.
- Arasteh H, Mashayekhi R, Goodarzi M, Motaharpour SH, Dahari M, Toghraie D. Heat and fluid flow analysis of metal foam embedded in a double-layered sinusoidal heat sink under local thermal non-equilibrium condition using nanofluid. *J Therm Anal Calorim*. 2019;138(2):1461–76.

34. Patankar S. Numerical heat transfer and fluid flow. Taylor & Francis; 2018.
35. Bahmani MH, Akbari OA, Zarringhalam M, Shabani GAS, Goodarzi M. Forced convection in a double tube heat exchanger using nanofluids with constant and variable thermophysical properties. *Int J Num Method Heat Fluid Flow*. 2019;30:3247–65.
36. Tian Z, Abdollahi A, Shariati M, Amindoust A, Arasteh H, Karimipour A, et al. Turbulent flows in a spiral double-pipe heat exchanger. *Int J Num Method Heat Fluid Flow*. 2019;30:39–53.
37. Seifi AR, Akbari OA, Alrashed AA, Afshary F, Shabani GAS, Seifi R, et al. Effects of external wind breakers of Heller dry cooling system in power plants. *Appl Therm Eng*. 2018;129:1124–34.
38. Wei M, Wu C, Zhou Y. Numerical simulation and experimental study on flow of polymer aqueous solution in porous jet nozzle. *Adv Polym Technol*. 2020. <https://doi.org/10.1155/2020/7580460>.
39. Bhatti M, Michaelides EE. Study of Arrhenius activation energy on the thermo-bioconvection nanofluid flow over a Riga plate. *J Therm Anal Calorim*. 2021;143(3):2029–38.
40. Abo-Elkhair R, Bhatti M, Mekheimer KS. Magnetic force effects on peristaltic transport of hybrid bio-nanofluid (AuCu nanoparticles) with moderate reynolds number: an expanding horizon. *Int Commun Heat and Mass Transf*. 2021;123(1):05228.
41. Amiri MH, Keshavarzi A, Karimipour A, Bahiraei M, Goodarzi M, Esfahani JA. A 3-D numerical simulation of non-Newtonian blood flow through femoral artery bifurcation with a moderate arteriosclerosis: investigating Newtonian/non-Newtonian flow and its effects on elastic vessel walls. *Heat Mass Transf*. 2019;55(7):2037–47. <https://doi.org/10.1007/s00231-019-02583-4>.
42. Somesaraee MT, Rad EA, Mahpeykar MR. Analytical investigation of simultaneous effects of convergent section heating of Laval nozzle, steam inlet condition, and nozzle geometry on condensation shock. *J Therm Anal Calorim*. 2018;133(2):1023–39.
43. Waqas H, Khan SU, Bhatti M, Imran M. Significance of bioconvection in chemical reactive flow of magnetized Carreau-Yasuda nanofluid with thermal radiation and second-order slip. *J Therm Anal Calorim*. 2020;140(3):1293–306.
44. Bagherzadeh SA, Jalali E, Sarafraz MM, Akbari OA, Karimipour A, Goodarzi M, et al. Effects of magnetic field on micro cross jet injection of dispersed nanoparticles in a microchannel. *Int J Numr Method Heat Fluid Flow*. 2019;30:2683–704.
45. Arain M, Bhatti M, Zeeshan A, Saeed T, Hobiny A. Analysis of arrhenius kinetics on multiphase flow between a pair of rotating circular plates. *Math Prob Eng*. 2020. <https://doi.org/10.1155/2020/2749105>.
46. Yousefzadeh S, Rajabi H, Ghajari N, Sarafraz MM, Akbari OA, Goodarzi M. Numerical investigation of mixed convection heat transfer behavior of nanofluid in a cavity with different heat transfer areas. *J Therm Anal Calorim*. 2019;140:1–25.
47. Rezaei B, Askari M, Shoushtari AM, Malek RAM. The effect of diameter on the thermal properties of the modeled shape-stabilized phase change nanofibers (PCNs). *J Therm Anal Calorim*. 2014;118(3):1619–29.
48. Bahiraei M, Heshmatian S, Goodarzi M, Moayedi H. CFD analysis of employing a novel ecofriendly nanofluid in a miniature pin fin heat sink for cooling of electronic components: effect of different configurations. *Adv Powder Technol*. 2019;30(11):2503–16.
49. Balduzzi F, Bianchini A, Maleci R, Ferrara G, Ferrari L. Critical issues in the CFD simulation of Darrieus wind turbines. *Renewable Energy*. 2016;85:419–35.
50. Wei W, Chen N, Zhang J, Zhang X. Design of an intelligent rapid nozzle cleaning control system for fused deposition modelling 3D printers. *Journal homepage: <http://ieta.org/Journals/IJHT>*. 2018;36(2):704–8.
51. Zhang L, Bhatti M, Michaelides EE. Thermally developed coupled stress particle–fluid motion with mass transfer and peristalsis. *J Therm Anal Calorim*. 2021;143(3):2515–24.
52. Shahid A, Huang H, Khalique C, Bhatti M. Numerical analysis of activation energy on MHD nanofluid flow with exponential temperature-dependent viscosity past a porous plate. *J Therm Anal Calorim*. 2021;143(3):2585–96.
53. Lu Y, Su X, Li J. A topology-alterative two-phase flow solver and its validation for a dynamic hydraulic discharge process. *J Hydraul Res*. 2019;57(5):607–22.
54. Kukutla PR, Prasad B, Tarigonda H, Reddy DR. Optimization of film hole row locations of a nozzle guide vane using network approach. *J Therm Anal Calorim*. 2020. <https://doi.org/10.1007/s10973-020-09841-2>.
55. Goodarzi M, Javid S, Sajadifar A, Nojoomizadeh M, Motaharipour SH, Bach Q-V, et al. Slip velocity and temperature jump of a non-Newtonian nanofluid, aqueous solution of carboxy-methyl cellulose/aluminum oxide nanoparticles, through a microtube. *Int J Numer Method Heat Fluid Flow*. 2019;29:1606–28.
56. Gheynani AR, Akbari OA, Zarringhalam M, Shabani GAS, Alnaqi AA, Goodarzi M et al. Investigating the effect of nanoparticles diameter on turbulent flow and heat transfer properties of non-Newtonian carboxymethyl cellulose/CuO fluid in a microtube. *Int J Numr Method Heat Fluid Flow*. 2019; 29(5):1699–1723. <https://doi.org/10.1108/HFF-07-2018-0368>
57. Ling J, Kurzawski A, Templeton J. Reynolds averaged turbulence modelling using deep neural networks with embedded invariance. *J Fluid Mech*. 2016;807:155–66.
58. de Oliveira AR, Molina EF, de Castro MP, Fonseca JLC, Rosanezi G, de Freitas F-P, et al. Structural and thermal properties of spray-dried methotrexate-loaded biodegradable microparticles. *J Therm Anal Calorim*. 2013;112(2):555–65.
59. Ji B, Luo X, Arndt RE, Peng X, Wu Y. Large eddy simulation and theoretical investigations of the transient cavitating vortical flow structure around a NACA66 hydrofoil. *Int J Multiph Flow*. 2015;68:121–34.

**Publisher's Note** Springer Nature remains neutral with regard to jurisdictional claims in published maps and institutional affiliations.